Monthly Notices
of the
ROYAL ASTRONOMICAL SOCIETY

MNRAS **436,** 1130–1141 (2013)
Advance Access publication 2013 September 25

doi:10.1093/mnras/stt1641

A fundamental metallicity relation for galaxies at $z = 0.84$–1.47 from HiZELS

John P. Stott,[1⋆] David Sobral,[2] Richard Bower,[1] Ian Smail,[1] Philip N. Best,[3] Yuichi Matsuda,[4,5] Masao Hayashi,[6] James E. Geach[7] and Tadayuki Kodama[4,8]

[1]*Institute for Computational Cosmology, Durham University, South Road, Durham DH1 3LE, UK*
[2]*Leiden Observatory, Leiden University, PO Box 9513, NL-2300 RA Leiden, the Netherlands*
[3]*SUPA, Institute for Astronomy, Royal Observatory of Edinburgh, Blackford Hill, Edinburgh EH9 3HJ, UK*
[4]*National Astronomical Observatory of Japan, 2-21-1 Osawa, Mitaka, Tokyo 181-8588, Japan*
[5]*The Graduate University for Advanced Studies (SOKENDAI), 2-21-1 Osawa, Mitaka, Tokyo 181-8588, Japan*
[6]*Institute for Cosmic Ray Research, The University of Tokyo, Kashiwa 277-8582, Japan*
[7]*Centre for Astrophysics Research, Science & Technology Research Institute, University of Hertfordshire, Hatfield AL10 9AB, UK*
[8]*Subaru Telescope, National Astronomical Observatory of Japan, 650 North Aohoku Place, Hilo, HI 96720, USA*

Accepted 2013 August 28. Received 2013 August 14; in original form 2013 June 27

ABSTRACT

We obtained Subaru FMOS observations of Hα emitting galaxies selected from the HiZELS, to investigate the relationship between stellar mass, metallicity and star formation rate (SFR) at $z = 0.84$–1.47, for comparison with the fundamental metallicity relation seen at low redshift. Our findings demonstrate, for the first time with a homogeneously selected sample, that a relationship exists for typical star-forming galaxies at $z \sim 1$–1.5 and that it is surprisingly similar to that seen locally. Therefore, star-forming galaxies at $z \sim 1$–1.5 are no less metal abundant than galaxies of similar mass and SFR at $z \sim 0.1$, contrary to claims from some earlier studies. We conclude that the bulk of the metal enrichment for this star-forming galaxy population takes place in the 4 Gyr before $z \sim 1.5$. We fit a new mass–metallicity–SFR plane to our data which is consistent with other high-redshift studies. However, there is some evidence that the mass–metallicity component of this high-redshift plane is flattened, at all SFR, compared with $z \sim 0.1$, suggesting that processes such as star formation-driven winds, thought to remove enriched gas from low-mass haloes, are yet to have as large an impact at this early epoch. The negative slope of the SFR–metallicity relation from this new plane is consistent with the picture that the elevation in the SFR of typical galaxies at $z \gtrsim 1$ is fuelled by the inflow of metal-poor gas and not major merging.

Key words: galaxies: abundances – galaxies: evolution – galaxies: star formation.

1 INTRODUCTION

Gas phase metallicity is a key parameter to constrain the current stage of galaxy evolution because it reflects the result of past star-forming activity and the history of both gas inflow and outflow of the system. The presence of a stellar mass–metallicity relation (sometimes referred to as the MZR) for star-forming galaxies was first observed by Lequeux et al. (1979), with more massive galaxies possessing higher gas metallicity, and this is now well established at $z \sim 0.1$ (e.g. Tremonti et al. 2004; Kewley & Ellison 2008). The origin of this relation is thought to be due to massive galaxies, with their deeper gravitational potential wells, being better able to hold on to their enriched gas, in the presence of strong star formation-driven winds, than their less massive counterparts (an idea first proposed by Larson 1974 in relation to elliptical galaxies; see also Arimoto & Yoshii 1987).

Tracking the evolution of the mass–metallicity relation of star-forming galaxies with redshift should help to illuminate the physical processes responsible for the peak in the volume averaged star formation rate (SFR) for galaxies at $z = 1$–2 and its subsequent downturn to the present day (e.g. Lilly et al. 1996; Madau et al. 1996; Sobral et al. 2013). The mass–metallicity relation of star-forming galaxies is generally observed to shift to lower metallicity with increasing redshift, relative to the $z = 0.1$ relation of Tremonti et al. (2004) (e.g. Savaglio et al. 2005; Erb et al. 2006; Maiolino et al. 2008; Lamareille et al. 2009; Pérez-Montero et al. 2009; Yabe et al. 2012; Zahid et al. 2013). This would suggest that galaxy metallicity evolves strongly from $z \gtrsim 1$ to the present.

⋆E-mail: j.p.stott@durham.ac.uk

However, instead of constituting an evolution, it has been suggested by Mannucci et al. (2010) that these results are due to the high-redshift samples having significantly higher SFRs. This is because the observed high-redshift galaxies are often ultraviolet (UV) selected from flux limited samples with high SFRs, even compared to the elevated specific star formation rate (sSFR) of typical galaxies at these epochs. The UV selection tends to bias against metal-rich/dusty galaxies while being complete for very metal poor galaxies. In fact, Mannucci et al. (2010) find that these high-redshift, high-SFR galaxies sit on the same 'Fundamental Metallicity Relation' (FMR; see also Lara-López et al. 2010, 2013; Cresci et al. 2012), a plane in mass–metallicity–SFR, as that of $z \sim 0.1$ galaxies from the Sloan Digital Sky Survey (SDSS; Abazajian et al. 2009). An extension to this FMR for low-mass galaxies was published in Mannucci, Salvaterra & Campisi (2011). The shape of the FMR is to first order a manifestation of the positive correlation of the metallicity with stellar mass at fixed SFR (i.e. the mass–metallicity relation) and a negative correlation with SFR at fixed stellar mass. The latter relation is thought to be because the inflowing fuel for star formation has its origins in the relatively metal-poor intergalactic medium (IGM; e.g. Finlator & Davé 2008). However, this is still a matter of some debate as, for a local sample of galaxies observed with integrated field spectroscopy, Sánchez et al. (2013) do not find evidence of a negative correlation between metallicity and SFR at fixed stellar mass.

A number of recent studies have attempted to confirm the presence of this FMR at $z \gtrsim 1$ with various high-redshift samples. For example, using a sample of highly star-forming ($>20\,\mathrm{M}_\odot\,\mathrm{yr}^{-1}$), $z \sim 1$ *Herschel* far-infrared selected galaxies, Roseboom et al. (2012) find that their galaxies are consistent with the SDSS FMR albeit with large scatter. At $z \sim 1.4$, Yabe et al. (2012) also find some agreement with the FMR when following up a highly star-forming ($>20\,\mathrm{M}_\odot\,\mathrm{yr}^{-1}$), photometrically selected sample, but again with a significant scatter compared with $z = 0.1$. Studies of small samples of gravitationally lensed systems by Richard et al. (2011), Wuyts et al. (2012) and Belli et al. (2013), in particular the latter, test the low-mass regime of the FMR at $1.0 < z < 3$ and again find some agreement with the local plane. However, it is clear that a well-defined sample of typical high-redshift galaxies that probes down to lower SFRs ($<10\,\mathrm{M}_\odot\,\mathrm{yr}^{-1}$) is required to take these comparisons further.

Investigations of the form of the FMR and its evolution are important to constrain models and simulations of galaxy evolution that invoke a feedback mechanism to regulate star formation, thought to be an important component in our understanding of galaxy evolution (e.g. Larson 1974; White & Rees 1978). In all but the most massive galaxies, where active galactic nuclei (AGN) are often invoked to suppress star formation (e.g. Bower et al. 2006), it is heating and winds from supernovae and massive stars that provide this regulation (e.g. Benson et al. 2003; Crain et al. 2009). Through the balance of star formation with feedback and the inflow of lower metallicity gas from the IGM, some recent models have managed to broadly reproduce the properties of the FMR at low redshift (e.g. Davé, Finlator & Oppenheimer 2011, 2012; Dayal, Ferrara & Dunlop 2013; Lilly et al. 2013).

Narrow-band Hα surveys provide a volume-selected sample (to an SFR limit) allowing for straightforward analysis of trends with SFR or mass (e.g. Sobral et al. 2011; Stott et al. 2013). The Hα emission line is less affected by dust obscuration than shorter wavelength star formation tracers (e.g. UV and [O II]). Beyond $z = 0.4$ Hα is redshifted out of the optical window, thus high-redshift studies of star formation have been limited to either using the obscuration-affected short wavelength tracers or studying small samples of Hα emitters from conventional near-infrared spectrographs. However, in the last five years wide-field, narrow-band surveys such as the High-redshift (Z) Emission Line Survey (HiZELS; Geach et al. 2008, 2012; Sobral et al. 2009, 2010, 2012, 2013; Garn et al. 2010; Stott et al. 2013) have started to provide large samples of Hα-selected galaxies (see also the studies of Villar et al. 2008; Ly et al. 2011). These narrow-band surveys produce emission line information over large areas of the sky and are thus able to probe both ends of the Hα luminosity and stellar mass functions of star-forming galaxies, required for an unbiased analysis of the star formation rate density (SFRD; e.g. Sobral et al. 2013).

HiZELS provides the large well-defined sample of star-forming galaxies at high redshift required to investigate the evolution of the FMR from the peak epoch of star formation ($z \sim 1$–2). In this paper we obtain gas phase metallicities for the HiZELS sources at $z = 0.84$ and 1.47, with the near-infrared Fiber Multi-Object Spectrograph (FMOS; Kimura et al. 2010) on the Subaru Telescope. This enables us, for the first time, to probe the mass, metallicity and SFRs of typical star-forming galaxies, in order to map out the equivalent of the FMR at this crucial epoch for galaxy evolution studies.

The structure of this paper is as follows. In Section 2 we describe the HiZELS sample, the FMOS observation data and the spectral line fitting. We then assess the SFR, metallicity and AGN content through emission line diagnostics and the stellar mass through the available broad-band data (Section 3). In Section 4 we compare the HiZELS mass–metallicity relation to that from other studies and then test for the presence of a plane in mass, metallicity and SFR at $z \sim 1$–1.5. Finally in Section 5, we discuss the implications of our findings in the context of galaxy evolution and the increase in the SFRD with redshift.

A Λ cold dark matter cosmology ($\Omega_\mathrm{m} = 0.27$, $\Omega_\Lambda = 0.73$, $H_0 = 70\,\mathrm{km\,s^{-1}\,Mpc^{-1}}$) is used throughout this work and all magnitudes are AB.

2 THE SAMPLE AND DATA

HiZELS (Geach et al. 2008; Sobral et al. 2013) is a Campaign Project using the Wide Field CAMera (WFCAM; Casali et al. 2007) on the United Kingdom InfraRed Telescope (UKIRT) which exploits specially designed narrow-band filters in the J and H bands (NB_J and NB_H), along with the $\mathrm{H_2S1}$ filter in the K band, to undertake panoramic, moderate depth surveys of emission line galaxies. HiZELS targets the Hα emission line redshifted into the near-infrared at $z = 0.84$, 1.47 and 2.23 using these filters. In addition, the UKIRT data are complemented by deeper narrow-band observations with Subaru Suprime-Cam NB921 imaging (Sobral et al. 2012, 2013) to obtain Hα emitting galaxies at $z = 0.4$ and the [O II] emission from the $z = 1.47$ Hα sample, as well as deeper WFCAM and Very Large Telescope near-infrared imaging through the $\mathrm{H_2S1}$ filter in selected fields. The survey is designed to trace star formation activity across the peak of SFRD and provide a well-defined statistical sample of star-forming galaxies at each epoch (see Best et al. 2010).

In this study we concentrate on the HiZELS $z = 0.84$ and 1.47 Hα emitters in the Cosmic Evolution Survey (COSMOS), Bootes and Elais-N1 fields, with the $z = 1.47$ galaxies being the primary subsample and the $z = 0.84$ being the secondary. These samples were observed with FMOS, a near-infrared fibre-fed multi-object spectrograph on the Subaru Telescope (Kimura et al. 2010). FMOS allows for the placement of up to 400 1.2 arcsec diameter fibres within a 30 arcmin diameter circular field of view and the light

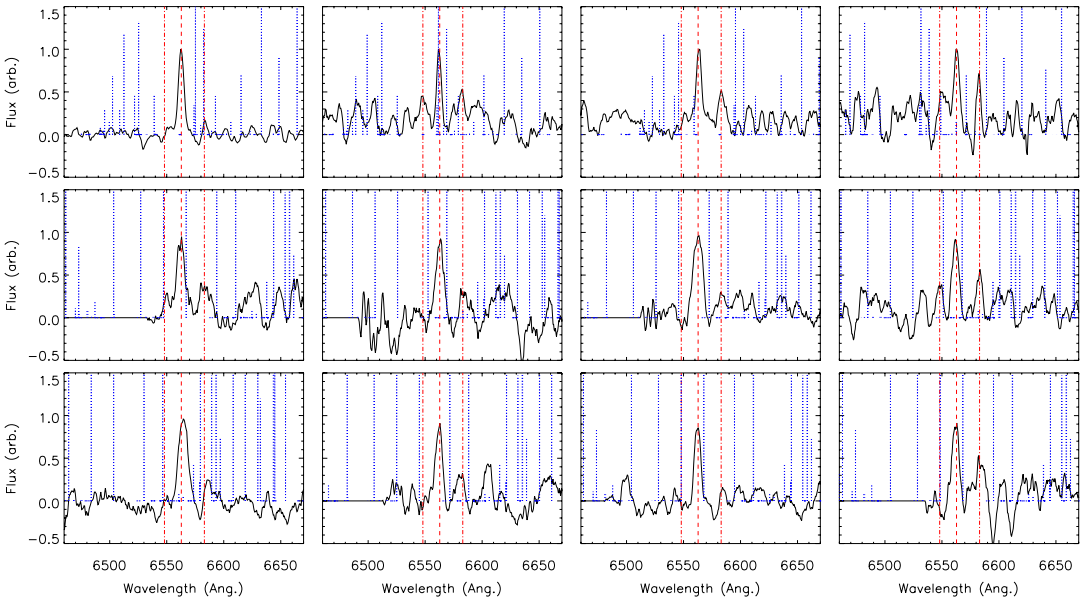

Figure 1. A selection of 12 spectra taken from the sample of 64 HiZELS-FMOS galaxies for which we recover both Hα and [N II] emission lines with, S/N > 5 and 2, respectively (see Section 2.3). The wavelength is given in the rest frame, the flux is normalized to the peak flux of the Hα emission line and a smoothing of 1.5 FMOS resolution elements has been applied (9 Å). The vertical dotted blue lines show the location of the sky lines, in the *observed frame*, from the Rousselot et al. (2000) catalogue and we have removed the FMOS OH suppression mask where it affects the data by dividing by the high noise values at their locations. The wavelengths of the Hα and [N II] (6548y Å and 6583 Å) spectral lines are marked by the dashed and dot–dashed red lines, respectively.

from these fibres is extracted as spectra by the two spectrographs (IRS1 and IRS2). A mirror mask is installed in the spectrographs for OH airglow suppression. The spectral coverage is from 0.9 to 1.8 μm which is divided into four 0.25 μm wide bands (*J*-Short, *J*-Long, *H*-Short and *H*-Long) with $R \approx 2200$, on average, in high-resolution mode.

The galaxies are drawn randomly from the HiZELS catalogues with the primary, $z = 1.47$, subsample observed with both the FMOS *H*-Long ($R = 2600$) filter, to measure Hα 6563 Å and [N II] 6583Å line fluxes, and the *J*-Long ($R = 1900$) filter, to obtain the [O III] 5007Å and Hβ 4861 Å fluxes. Those in the secondary, $z = 0.84$, subsample are observed using the *J*-Long filter again to obtain Hα and [N II].

In total we observed six FMOS fields of view, integrating for one hour each in both the *J*-Long and *H*-Long wavebands on the nights of 2012 May 4 and 5 in 0.6–0.8 arcsec optical seeing conditions (Proposal ID: S12A-062). These are divided into two COSMOS fields, three Bootes fields and one Elais-N1 field. In total we target 381 $z = 0.84$ and 1.47 Hα emitters (68 and 313, respectively). The remainder of the FMOS fibres were used to target $z = 2.23$ galaxies for studies of [O III] and [O II] 3727Å, non-HiZELS AGN targets, flux calibration stars or were placed on the sky to improve the removal of the atmospheric OH lines. The data for these additional targets are not discussed further in this paper.

For the observations we use the cross-beam switch (CBS) technique in which two fibres are allocated to one source and the telescope is offset between two positions so that either of the two fibres observes the source and the other observes sky, for improved sky subtraction at near-infrared wavelengths (e.g. see Rodrigues et al. 2012). This means that up to 200 sources can be observed at once. This sampling is appropriate to the target density of the HiZELS survey so the choice of CBS mode is not a limitation. The advantages of the CBS method are that targets are observed for 100 per cent of the time and that sky subtraction is less affected by the temporal and spatial variation of sky brightness.

2.1 Data reduction

The data are reduced with the Subaru FMOS reduction pipeline, FMOS Image-Based REduction Package (FIBRE-PAC; Iwamuro et al. 2012). FIBRE-PAC is a combination of IRAF tasks and C programs using the CFITSIO library (Pence 1999).

The raw data consist of science frames, dome flats and Th–Ar spectral calibration arcs. The details of the reduction process can be found in the FIBRE-PAC paper (Iwamuro et al. 2012) but we outline the key steps here. In the initial preparation the data are first flat fielded and bad pixels removed. Corrections are applied to remove spatial and spectral distortions present and then wavelength calibration is performed. An initial background subtraction is then achieved using the ABAB nodding pattern of the telescope to perform an A-B sky subtraction. Further bad pixel, detector cross-talk, bias difference, distortion, residual background and sky corrections are then applied. The 2D spectra are then combined, which in CBS mode means inverting and adding the negative B spectra to the A spectra. The final step is an initial flux calibration (see Section 2.2) using the spectra from a number of fibres which were set to observe stars with known near-infrared spectral energy distributions [SEDs; i.e. those with the Two Micron All Sky Survey (2MASS) photometry; Skrutskie et al. 2006] in combination with template stellar spectra from Rayner, Cushing & Vacca (2009) and accounting for the effects of atmospheric absorption. The fully reduced 1D spectra corresponding to each fibre pair are then extracted from the 2D frame. A selection of individual, e.g., spectra used for the main sample in this paper, covering the full range in signal-to-noise ratio (S/N), are provided in Fig. 1.

2.2 Spectral line fitting

The advantage of the HiZELS survey is that the redshift of the galaxies in our sample is known to $\delta z \sim \pm 0.015$ and therefore it is not necessary to search the entire wavelength range for emission

lines. We take the 1D spectra, smoothed over 6 Å (corresponding to 5 spectral pixels, appropriate to the spectral resolution of ∼2200), and identify the emission lines that fall in the wavelength range of the HiZELS narrow-band filters. These emission lines are fitted with a single Gaussian profile in order to extract their total flux. We extract both the Hα 6563 Å and [N II] 6583 Å emission lines for the $z = 1.47$ and 0.84 samples from the *H*-Long and *J*-Long observations, respectively, with these lines easily resolved from each other in high-resolution mode. For the $z = 1.47$ galaxies we also fit to any spectral lines present at the wavelengths corresponding to Hβ 4861 Å and [O III] 5007 Å line emission within the appropriate *J*-Long observations.

As with all near-infrared observations these spectra are affected by OH sky lines that were not fully removed in the data reduction pipeline. A further important factor with FMOS is that there is also a mirror mask to suppress the strongest OH airglow lines. This means that in the regions where there is a strong sky line present the flux has been completely removed. Because of the sky lines and the OH suppression it is difficult to extract real spectral lines that are in the vicinity of the sky affected regions, with some potentially being completely obscured in regions where the OH suppression is most aggressive (see also Yabe et al. 2012). We flag galaxies with spectral lines that are strongly affected by the OH suppression, i.e. with central wavelengths that fall within one FMOS resolution element (6 Å) of a line in the OH suppression mask, these galaxies are then removed from any analysis which requires that specific line.

After obtaining initial fluxes from the FMOS spectra we then apply a further flux calibration based on the known Hα HiZELS narrow-band fluxes of the galaxies. As well as providing a more accurate flux calibration, this accounts for the 1.2 arcsec diameter FMOS fibres which potentially means that not all of the Hα emission for a given galaxy detected in HiZELS will be observed by FMOS. For example, the Hα emission from the galaxy may extend outside of this diameter, as from Stott et al. (2013) we know that the average broad-band half-light radii of the HiZELS galaxies at these redshifts is ∼3–4 kpc or ∼0.5 arcsec. Another related possibility is that the fibres are not centred exactly on the peak of the Hα emission. We use an individual aperture correction for each galaxy, which is the ratio of the HiZELS narrow-band flux to the Hα + [N II] flux measured from the FMOS spectroscopy. The median value of this aperture correction, for the full sample of 64 galaxies with detected Hα and [N II] used throughout this paper (see Section 2.3), is 2.6 ± 0.2 (in agreement with that found by Roseboom et al. 2012; Yabe et al. 2012; Matsuda et al. 2011).

We calculate the S/N of the Hα measurements from the noise image produced by the data reduction pipeline and the variance of the background of the calibrated spectra. We only consider Hα lines with an S/N> 5, which corresponds to a flux of $\sim 4 \times 10^{-17}$ erg cm^{-2} s^{-1} for both the *J*-Long and *H*-Long setups, in agreement with both the values quoted for 1 h of integration in the FMOS documentation and with the limiting flux of the input HiZELS narrow-band sample. The corresponding S/N = 5 SFR limits for $z = 0.84$ and 1.47 are therefore ∼1 and $\sim 5\,M_\odot$ yr^{-1}, respectively, assuming a Kennicutt (1998) star formation law, corrected to a Chabrier (2003) initial mass function (IMF) and a dust extinction at the Hα wavelength, $A_{H\alpha} = 1$ mag (see Section 3). We note here that recent, similar studies with FMOS have only probed down to $\sim 1 \times 10^{-16}$ erg cm^{-2} s^{-1} ($\gtrsim 20\,M_\odot$ yr^{-1} at $z \sim 1.5$) due to the use of the FMOS low-resolution mode (i.e. Roseboom et al. 2012; Yabe et al. 2012) rather than the more sensitive high-resolution mode utilized here.

An additional consideration when studying Hα and Hβ emission lines is that they are superimposed on the stellar Balmer absorption line features. As we do not detect significant continuum in either our individual or stacked galaxy spectra we cannot assess this directly. However, following Yabe et al. (2012) we note that both Savaglio et al. (2005) and Zahid, Kewley & Bresolin (2011) find this effect to be small, typically requiring a correction of 1–4 Å to the equivalent width (EW) of the emission line. HiZELS has a rest-frame EW lower limit of 25 Å and a median rest-frame EW of ∼100 Å and thus the effect of the Balmer absorption is negligible by comparison. We therefore choose not to include a correction for this effect.

2.3 Sample statistics and accounting for non-detections

Of the 381 $z = 0.84$ and 1.47 HiZELS Hα emitters targeted, we recover Hα emission above S/N = 5 for 193 (∼50 per cent) and Hα + [N II] for 64 (∼33 per cent) of these (with an S/N = 2 detection threshold for [N II]). Of the 152 for which we recover $z = 1.47$ Hα emission in the *H*-Long set-up, we detect [O III] in 67 and Hβ in 13 (with an S/N = 2 detection threshold for both) with the *J*-Long. We show some example spectra around Hα and [N II] in Fig. 1. In Fig. 2 we present the rest-frame wavelength median stacks normalized to

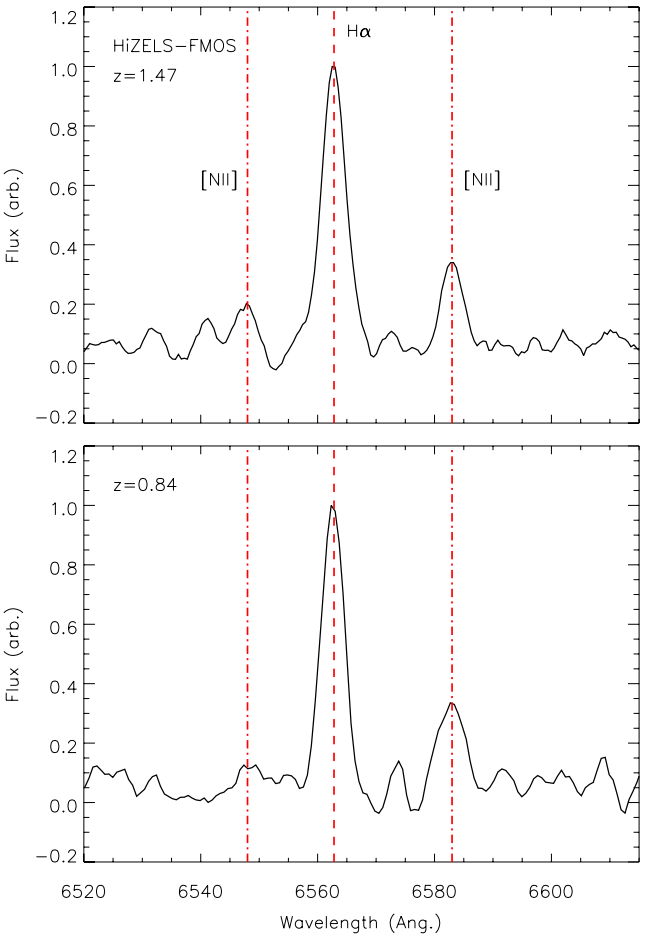

Figure 2. A rest-frame stack of the spectra of the $z = 1.47$ and 0.84 Hα emitting galaxies with the wavelength of the Hα and [N II] (6548 Å and 6583 Å) spectral lines marked by the dashed and dot–dashed red lines. The stacked ratios of [N II]/Hα are 0.36 ± 0.03 and 0.34 ± 0.02 for $z = 0.84$ and 1.47, respectively, corresponding to the metallicities $12 + \log(O/H) = 8.65 \pm 0.02$ and 8.63 ± 0.02 (assuming the conversion of Pettini & Pagel 2004), consistent with the solar value of 8.66 ± 0.05 (Asplund et al. 2004).

their peak flux density for the $z = 0.84$ and 1.47 Hα emitters which clearly also shows the [N II]6583 Å line. However, in the entire $z = 1.47$ sample there are only three galaxies with a measurement of all four lines (Hα, Hβ, [N II] and [O III]) above the stated S/N thresholds. The main reason for this is that the Hβ line, and to a lesser extent the [N II] and [O III] lines, are in wavelength ranges that are strongly affected OH lines (see also Yabe et al. 2012).

It is important to assess the reasons for the 188 missing HiZELS Hα emitters in order to characterize the HiZELS narrow-band sample. The minimum flux of the HiZELS narrow-band sample is $\sim 4 \times 10^{-17}$ erg cm^{-2} s^{-1}, the same as our FMOS S/N = 5 detection threshold, so perhaps this is due to extended flux being missed by the FMOS fibres, a fibre misalignment or the lines being coincident with an OH sky line (see Section 2.2), some of the sources may have fallen below this threshold or have been masked from the analysis. The possibility that we are missing galaxies due to low observed flux is confirmed when we consider how the fraction of non-detections varies with the HiZELS narrow-band flux. We detect Hα in ∼85 per cent of the galaxies with a narrow-band flux greater than $\sim 4 \times 10^{-16}$ erg cm^{-2} s^{-1} but only recover ∼45 per cent of those near the detection limit of $\sim 4 \times 10^{-17}$ erg cm^{-2} s^{-1}. If we now consider all 'detections' of potential Hα (i.e. where a line was fitted to a spectral feature in the correct wavelength range, not associated with an OH sky line) above an S/N = 2 threshold this accounts for 101 of the missing galaxies (∼50 per cent). We therefore conclude that half of the Hα non-detections are due to galaxies with a low observed flux compared to their narrow-band flux (see Section 2.2). The remaining 87 galaxies that are undetected in Hα account for just ∼20 per cent of the total galaxies targeted.

To measure the effect the OH sky lines have on Hα detection, we assess the percentage of the wavelength coverage of the narrow-band filters affected by strong OH lines and the FMOS OH suppression. To quantify this we use the OH sky line catalogue of Rousselot et al. (2000) and the wavelengths of the FMOS OH suppression. From our experience with the FMOS spectra the strong, OH suppressed, sky lines and those with a relative intensity >20 in the Rousselot et al. (2000) catalogue have a destructive effect on the spectra. Taken in combination, the percentage of the NB$_J$ and NB$_H$ filters affected by sky lines with a relative intensity >20 (Rousselot et al. 2000), assuming the FMOS resolution of 6 Å, is ∼20 per cent. As this agrees with the percentage of unaccounted-for non-detections of Hα, then this is most likely the reason for their absence from the HiZELS-FMOS sample.

The galaxies with detected Hα but without [N II] emission will have a greater impact on our study of the metallicity, which is determined from the flux ratio [N II]/Hα, with unaccounted-for non-detections potentially acting to bias our sample to higher metallicities. The two major reasons for the non-detection of [N II] are that the line itself is faint or that it is coincident with an OH sky line, which are removed from our analysis (see Section 2.2). To test the relative numbers of these we compare the [N II] redshifts of all of the 193 galaxies for which we detect Hα above an S/N = 5 to the sky line catalogue of Rousselot et al. (2000) and the FMOS OH suppression of the strong sky lines. To quantify the effect of the OH sky lines we calculate the number of non-detected [N II] lines that would fall within 9 Å (1.5 times the spectral resolution of FMOS at these wavelengths) of an OH line, with a relative intensity >20 as defined in the Rousselot et al. (2000) catalogue. The median spectral separation to a sky line from the [N II] wavelength of a galaxy which is detected in Hα but undetected in [N II] is 6 Å (i.e. the resolution of FMOS), whereas for those with detected [N II] this spectral separation is 16 Å. This clearly shows a strong link between the presence of atmospheric OH emission and the non-detection of [N II]. In total 70 per cent of the [N II] non-detections lie within 9 Å of an atmospheric OH line, which we therefore conclude is the reason for their non-detection. There may also be some contamination from non-Hα emission line galaxies for which we would never detect [N II] although the majority of these should be removed by the sample cleaning processes described in Sobral et al. (2013). In the Sections 3.2, 4.1 and 4.2 analyses we include the small effect which the remaining 30 per cent (44) of the [N II] non-detections have on the [N II]/Hα flux ratio and metallicity.

We also quantify the missing [O III] and Hβ emitters in the same way. As with [N II], 70 per cent of the missing [O III] and Hβ emitters lie within 9 Å of an atmospheric OH line which we again attribute as the reason for the majority of the non-detections of these lines. The median spectral separation to a sky line for a non-detected [O III] or Hβ source is again 6 Å, with the detected sources having a median spectral separation of 14 and 24 Å, respectively.

3 ANALYSIS

3.1 Dust extinction and AGN fraction

For the 13 galaxies with detections of both Hα and Hβ, plus the upper limits from the non-detections of Hβ (defined by the detection threshold, S/N = 2) for the remaining Hα detections that are not affected by sky lines, it is possible to estimate the average dust extinction via the Balmer decrement. The median Balmer decrement, including the upper limits, is found to be 4.2 ± 0.6. This is converted to an average dust extinction at the V-band wavelength, $A_V = 1.3 \pm 0.2$, assuming an intrinsic Hα/Hβ ratio of 2.86 from Case B recombination (Osterbrock 1989) and a Calzetti et al. (2000) reddening curve using the same technique as Domínguez et al. (2013) and Momcheva et al. (2013), which accounts for the difference between the extinction derived from the nebula emission and that from the stellar continuum. This translates to an Hα extinction, $A_{\rm H\alpha} = 1.1 \pm 0.2$.

We also estimate the dust extinction by performing a mean average of the Balmer decrement over the galaxies with detected Hβ and a mean stacked spectra at the Hβ wavelength of the non-detections. This method yields $A_V = 1.4 \pm 0.3$ and $A_{\rm H\alpha} = 1.1 \pm 0.3$, in agreement with the median of the detections and upper limits above. These results are entirely consistent with the average $A_{\rm H\alpha} = 1$ measured by Garn et al. (2010) for the HiZELS sample and used in both Sobral et al. (2013) and Stott et al. (2013) and which we now adopt for the remainder of this paper for consistency with those studies. Unfortunately, the number of combined Hα and Hβ detections in the HiZELS-FMOS sample is too small to test correlations between $A_{\rm H\alpha}$ and SFR or stellar mass.

As HiZELS is an emission line survey, some fraction of the galaxy sample will be AGN dominated. The ratios of [N II]/Hα and [O III]/Hβ lines are plotted against each other in a Baldwin, Phillips and Terlevich (BPT) diagram (Baldwin, Phillips & Terlevich 1981) to assess the AGN fraction of the HiZELS sample at $z = 1.47$ (Fig. 3). As stated in Section 2.3 there are only three galaxies with all four Hα, Hβ, [N II] and [O III] lines present above their detection thresholds. In order to increase the number of galaxies we also include upper limit data points from those with three lines either Hα, Hβ and [O III] (13 galaxies) or Hα, Hβ and [N II] (seven galaxies) with the upper limits defined by the detection threshold for the emission lines (S/N = 2). Finally, we include 15 galaxies with no detected Hβ emission for which we have estimated Hβ through the Hα flux assuming $A_{\rm H\alpha} = 1$ and Case B as above.

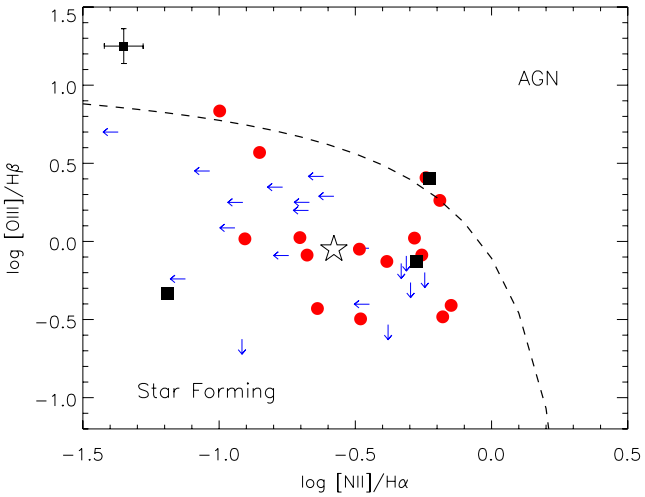

Figure 3. The BPT diagram (Baldwin et al. 1981) for the $z = 1.47$ HiZELS-FMOS sources. The dashed line is the demarcation between starbursts and AGN from Kewley et al. (2001). The filled black squares represent galaxies with all four emission lines, i.e. Hα, Hβ, [N II] and [O III], the upper limits (arrows) represent those with three lines that are missing either [O III] or [N II]. The filled red circles are those missing Hβ for which we have estimated Hβ through the Hα flux, assuming $A_{\rm H\alpha} = 1$ (see Section 3.1). The typical error is shown in the top-left corner of the plot. This demonstrates that the fraction of HiZELS galaxies that occupy the same region of the BPT diagram as AGN is ∼10 per cent, in agreement with other studies (e.g. Garn et al. 2010). The median values of [N II]/Hα and [O III]/Hβ are marked by a star which is clearly in the normal star-forming region of the diagram.

We assess the AGN content by considering the positions of the galaxies in the BPT diagram relative to the Kewley et al. (2001) line, often used as a demarcation between AGN (above) and starbursts (below). For our BPT sample of the HiZELS-FMOS galaxies at $z = 1.47$, which include those with all four lines, upper limits and estimated Hβ, 8 per cent ±5 are potential AGN in the Kewley et al. (2001) definition. If we look at the entire 64 galaxies with detections of both Hα and [N II] a further two galaxies have a flux ratio log [N II]/H$\alpha > 0.2$, which means they are most probably AGN in the Kewley et al. (2001) definition (see Section 4.2.1), giving a total AGN fraction of 8 per cent ±3. We note that the median BPT position of this sample, marked in Fig. 3, is well within the region of the diagram occupied by star-forming galaxies. In other independent analyses of the HiZELS survey, Garn et al. (2010) and Sobral et al. (2013) estimate that 5–15 per cent of the $z = 0.84$ and ∼15 per cent of the $z = 1.47$ galaxies are AGN through their observed SEDs and emission line ratios, consistent with our estimate. As we do not have the required spectral line information to assess the AGN content of each individual galaxy and the potential AGN identified are only a small fraction of the total, which lie very close to the Kewley et al. (2001) line, we do not exclude them from our analysis. We discuss the effect of low level AGN activity on our metallicity analysis in Section 3.2.

3.2 Stellar mass, SFR and metallicity

To assess the presence of the FMR at $z \sim 0.84$–1.47 we need to obtain reliable estimates of the mass, SFR and metallicity for the galaxies in the HiZELS-FMOS sample. The stellar masses are computed by fitting SEDs to the rest-frame UV, optical and near-infrared data available [*FUV*, *NUV*, *U*, *B*, *g*, *V*, *R*, *i*, *I*, *z*, *Y*, *J*, *H*, *K*, 3.6, 4.5, 5.8 and 8.0 μm collated in Sobral et al. (2013), and see references therein], following Sobral et al. (2011) and the reader is referred to that paper for more details. The SED templates are generated with the Bruzual & Charlot (2003) package using Charlot & Bruzual (unpublished manuscript, 2007) models, a Chabrier (2003) IMF, and an exponentially declining star formation history with the form $e^{-t/\tau}$, with τ in the range 0.1 Gyr to 10 Gyr. The SEDs were generated for a logarithmic grid of 200 ages (from 0.1 Myr to the maximum age at each redshift being studied). Dust extinction was applied to the templates using the Calzetti et al. (2000) law with $E(B - V)$ in the range 0 to 0.5 (in steps of 0.05), roughly corresponding to $A_{\rm H\alpha} \sim 0$–2. The models are generated with different metallicities, including solar; the reader is referred to Sobral et al. (2011) and Sobral et al. (in preparation) for further details. For each source, the stellar mass is computed as the median of stellar masses of the solutions which lie within 1σ of the best fit.

The SFRs for the HiZELS-FMOS sample are calculated from the aperture-corrected FMOS Hα luminosity and the relation of Kennicutt (1998) corrected to a Chabrier (2003) IMF [SFR($M_\odot$ yr^{-1}) = $4.4 \times 10^{-42} L_{\rm H\alpha}$(erg s^{-1})], assuming a dust extinction $A_{\rm H\alpha} = 1$ mag (see Section 3.1 for Balmer decrement analysis and Sobral et al. 2013).

The gas phase abundance of Oxygen [12 + log (O/H)] for the sample can be estimated from the ratio of the [N II] to Hα lines (Alloin et al. 1979; Denicoló, Terlevich & Terlevich 2002; Kewley & Dopita 2002). This is often referred to as the N2 method, where

$$\mathrm{N2} = \log(f_{\rm [N\,II]}/f_{\rm H\alpha}). \quad (1)$$

The median value of N2 for our sample (including the upper limits, assuming [N II] value is that of the S/N = 2 detection threshold) is 0.32 ± 0.03. To convert from N2 to oxygen abundance we use the conversion of Pettini & Pagel (2004), which is appropriate for high-redshift star-forming galaxies, where

$$12 + \log(\mathrm{O/H}) = 8.9 + 0.57 \times \mathrm{N2}. \quad (2)$$

The median metallicity of the HiZELS-FMOS sample, for those with detected [N II], is found to be 12 + log (O/H) = 8.71 ± 0.03. If we include the 44 non-detections of [N II] not affected by the OH sky lines (the 30 per cent of non-detections discussed in Section 2.3), then this median metallicity falls by 0.09 dex to 12 + log (O/H) = 8.62 ± 0.02. These values are in agreement with the $z = 1.47$ and 0.84 Hα emitter stacks featured in Fig. 2, where 12 + log (O/H) = 8.63 ± 0.02 and 8.65 ± 0.02, respectively, and all are consistent with the solar value of 8.66 ± 0.05 (Asplund et al. 2004).

The presence of unaccounted-for AGN may act to bias our metallicities to higher values due to their enhanced N2 values, with both Wright et al. (2010) and Newman et al. (2013) finding that at $z > 1$ the region of the BPT diagram at the boundary between star-forming galaxies and AGN contains some composite systems with spatially concentrated AGN imbedded within a star-forming galaxy. However, we note that in the case of Newman et al. (2013), their typical [O III]/Hβ values are significantly higher (log [O III]/H$\beta \sim 0.5$) compared to our median (log [O III]/H$\beta \sim 0$, see Fig. 3), which implies a higher AGN contribution to their sample. We can quantify the effect of this potentially hidden AGN contamination by performing simple cuts in the N2 value regardless of the [O III]/Hβ ratio. If we remove all galaxies with N2 > -0.2 then the median metallicity of our sample becomes 8.59 ± 0.02, leaving the result relatively unaffected. However, if we perform a more extreme cut at N2 $= -0.3$, then this value falls to 8.55 ± 0.02. This simple cut assumes that all galaxies with N2 ratios in excess of these values are AGN but if we instead randomly removed 50 per cent of the galaxies with N2 > -0.2 (-0.3) then the median metallicity (averaged over

1000 resamplings) is 8.59 ± 0.02 (8.58 ± 0.02). These values agree with our median metallicity for the full sample to within $\sim 1\sigma$ and therefore we conclude that our results are robust to the presence of hidden AGN.

4 RESULTS

4.1 The mass–metallicity relation

The mass–metallicity relation for our combined sample of $z = 0.84$ and 1.47 HiZELS-FMOS galaxies is plotted in Fig. 4, along with similar studies for comparison. We plot the median metallicity values for the sample (including the upper limits from the [N II] non-detections, see Section 2.3) in bins of 0.5 dex in mass with their associated standard errors. We also produce median stacks by combining the detected and [N II] upper limit spectra for each bin in mass and find that the resultant mass–metallicity relation is entirely consistent with the median values. The HiZELS-FMOS mass ranges and median metallicity values from Fig. 4 and those from the median stacks are presented in Table 1. We include a fit to the medians of the combined HiZELS-FMOS detected [N II] data and the upper limits of the form

$$12 + \log(\mathrm{O/H}) = -0.0864\,(\log M_\star - \log M_0)^2 + K_0 \qquad (3)$$

as used by Maiolino et al. (2008) to describe the mass–metallicity relations in their study of $z \sim 0.1-3.5$ galaxies [although we note that in their paper they use a Salpeter (1955) IMF and their own metallicity calibration]. The best-fitting values are $\log M_0 = 10.29 \pm 0.31$ and $K_0 = 8.64 \pm 0.03$. We also perform a linear fit to our data of the form

$$12 + \log(\mathrm{O/H}) = \alpha(\log \mathrm{M}_\star) + \beta, \qquad (4)$$

Table 1. The mass–metallicity relation data for the HiZELS-FMOS sample which includes the [N II] upper limits. The stellar mass range corresponds to the bin width and the metallicities are given as both the median values with their associated standard errors and the metallicity calculated from median stacking of all galaxies in the mass range. The number of galaxies per bin is also displayed.

$\log(M_\star/\mathrm{M}_\odot)$	Median $12 + \log(\mathrm{O/H})$	Stack $12 + \log(\mathrm{O/H})$	No. of gal.
9.0–9.5	8.53 ± 0.05	8.49 ± 0.02	19
9.5–10.0	8.64 ± 0.05	8.66 ± 0.02	35
10.0–10.5	8.64 ± 0.05	8.63 ± 0.02	32
10.5–11.0	8.62 ± 0.07	8.58 ± 0.02	17

which yields $\alpha = 0.077 \pm 0.050$ and $\beta = 7.85 \pm 0.05$. We compare the HiZELS-FMOS fits to the Kewley & Ellison (2008), $z = 0.07$; Savaglio et al. (2005), $z = 0.7$; Erb et al. (2006), $z = 2.2$; and the Maiolino et al. (2008), $z = 3.5$ data set, which appear to be progressively lower in metallicity with increasing redshift. For consistency with our analysis, the masses are corrected to a Chabrier (2003) IMF and to the Pettini & Pagel (2004) metallicity calibration, using the equations from Pettini & Pagel (2004) and Maiolino et al. (2008). From this we can see that our results are in remarkable agreement with the 'local', $z = 0.07$ SDSS relation of Kewley & Ellison (2008), which is very similar to the SDSS study of Tremonti et al. (2004). Our results are therefore systematically higher in metallicity than the $z = 0.7-3.5$ studies of Savaglio et al. (2005), Erb et al. (2006) and Maiolino et al. (2008) showing no evolution in redshift for the mass–metallicity relation of the star-forming population.

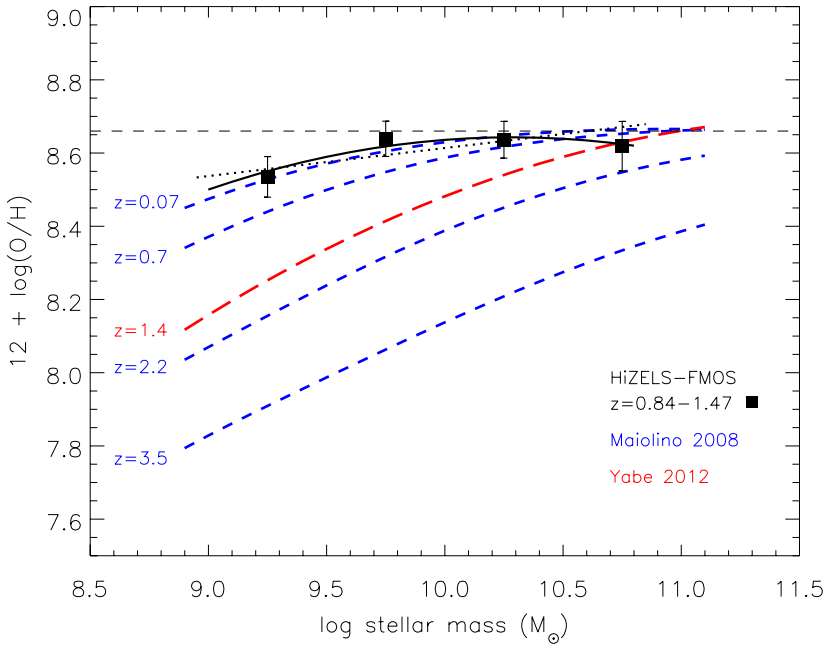

Figure 4. The median mass–metallicity relation for our combined $z = 0.84$–1.47 HiZELS-FMOS sample (black squares), including the upper limits from the non-detections of [N II], in bins of mass with *standard error* bars shown. The solid and dotted black lines are second order (see equation 3) and linear fits to this relation. The dashed blue lines are the Maiolino et al. (2008) fits to the Kewley & Ellison (2008), $z = 0.07$; Savaglio et al. (2005), $z = 0.7$; Erb et al. (2006), $z = 2.2$; and their own $z = 3.5$ data sets corrected to a Chabrier (2003) IMF and to the Pettini & Pagel (2004) metallicity calibration, for consistency with our data. The long dashed red line is taken from the Yabe et al. (2012) sample of $z = 1.4$ star-forming galaxies, which is most relevant to our sample, corrected to a Chabrier (2003) IMF. The black dashed horizontal line is the solar value of 8.66 (Asplund et al. 2004). The HiZELS-FMOS mass–metallicity relation is in remarkable agreement with the 'local', $z = 0.07$ SDSS relation of Kewley & Ellison (2008) and is systematically more metal rich than other samples, which we conclude is due to the significantly higher SFR probed in those studies, which we illustrate in Fig. 5.

The most relevant study to compare with our data is Yabe et al. (2012), which is a sample of photometrically selected $z = 1.4$ galaxies, albeit with significantly higher SFR than the HiZELS-FMOS sample $>20\,M_\odot\,yr^{-1}$. The Yabe et al. (2012) line is again systematically lower than the HiZELS-FMOS line by $\sim$0.3 dex at $10^{10}\,M_\odot$. The majority of our HiZELS-FMOS sample are at $z = 1.47$ so this discrepancy may be explained by the lower SFRs probed by our sample. This is in line with the FMR work of Mannucci et al. (2010) who find that even high-redshift galaxies sit on the local relation once their enhanced SFR, due in part to both selection effects and the rise in the typical sSFR with redshift, has been taken into account. The presence of the FMR at $z = 0.84$–1.47 is investigated in Section 4.2. We note that the slope of the mass–metallicity relation for our sample is also flattened relative to that of the comparison studies at similar z, which is discussed further in Section 4.2.

4.2 The fundamental metallicity relation

In this section we combine the mass, metallicity and SFR of the galaxies in our HiZELS-FMOS sample to investigate whether a plane such as the FMR of Mannucci et al. (2010) exists at $z \sim 1$–1.5 in order to discover whether a balance of gas inflow and outflow has already been set up at this redshift. Fig. 5 displays the mass–metallicity–SFR information for the HiZELS-FMOS sample. We include the SDSS derived FMR of Mannucci et al. (2010), corrected to the Pettini & Pagel (2004) metallicity calibration using the equations from Pettini & Pagel (2004) and Maiolino et al. (2008), for consistency with HiZELS-FMOS (see Table 2). Also plotted are the $z \sim 2$ observations of Erb et al. (2006) which are an excellent comparison sample to illustrate the argument of Mannucci et al. (2010). The top panel of Fig. 5 is a 3D representation of this plane to display its general form, with the FMOS observations as individual points. For ease of comparison we also include the two lower plots which are the mass–metallicity (left) and the SFR–metallicity (right) projections of the FMR, with the median values of the HiZELS-FMOS data (including the upper limits due to the non-detections of [N II]) plotted with their associated standard deviations to represent the scatter (cf. the standard errors in Fig. 4). As in Fig. 4 the lower-left panel shows that the mass–metallicity relation of the HiZELS-FMOS sample lies above that of Erb et al. (2006) but both lie within the span of values we include from the Mannucci et al. (2010) FMR. However, the SFR–metallicity relation (lower-right panel) shows that in fact the Erb et al. (2006) sample is highly star forming and is now in agreement with the HiZELS-FMOS sample. We perform a linear fit to the negative trend between SFR and metallicity of the form

$$12 + \log(\mathrm{O/H}) = \gamma(\log \mathrm{SFR}) + \delta, \quad (5)$$

which yields $\gamma = -0.175 \pm 0.066$ and $\delta = 8.73 \pm 0.06$.

From Fig. 5 we can see that the HiZELS-FMOS galaxies share the parameter space with both the low-redshift FMR of Mannucci et al. (2010) and the $z \sim 2$ observations of Erb et al. (2006). This FMOS observed, HiZELS sample therefore bridges the gap between the SDSS and $z \sim 2$ observations and demonstrates evidence of an FMR in place at $z \sim 1.5$.

4.2.1 Residuals about the FMR

To further demonstrate how the HiZELS-FMOS data compare to the SDSS FMR, in the upper two panels of Fig. 6 we plot the difference between the measured metallicity of the HiZELS-FMOS galaxies and the metallicity predicted by the $z \sim 0.1$ FMR [using the stellar masses and SFRs of our HiZELS-FMOS sample in the Pettini & Pagel (2004) version of the Mannucci et al. 2010 FMR, see Table 2], hereafter $\Delta[12 + \log(\mathrm{O/H})]_{\mathrm{M10}}$. In the upper-left panel of Fig. 6 $\Delta[12 + \log(\mathrm{O/H})]_{\mathrm{M10}}$ is plotted against stellar mass and in the upper right against SFR. From this plot one can see that the HiZELS-FMOS observations lie close to the $z \sim 0.1$ FMR with the median $\Delta[12 + \log(\mathrm{O/H})]_{\mathrm{M10}}$ being 0.04 with a scatter of 0.4 dex, showing good evidence that there is such a plane in place at $z = 1$–1.5. We note that the true scatter may be larger as we have included the upper limits. The scatter around the FMR is significantly larger than that seen at $z \sim 0.1$ by Mannucci et al. (2010) of 0.05 dex but this is in part due to the observed negative trend between $\Delta[12 + \log(\mathrm{O/H})]_{\mathrm{M10}}$ and the stellar mass. Also included in this plot are the binned values of the Erb et al. (2006) sample and the individual values from the lensed galaxy samples of Richard et al. (2011), Wuyts et al. (2012), Christensen et al. (2012) and Belli et al. (2013) at $z \sim 1.0$–3.0 with $\log(M_\star/M_\odot) > 8.5$ and $\log(\mathrm{SFR}[M_\odot\,yr^{-1}]) > 0.1$ to match the HiZELS-FMOS sample. These are all converted to the Pettini & Pagel (2004) metallicity calibration using the equations from Pettini & Pagel (2004) and Maiolino et al. (2008) and, where required for Richard et al. (2011), a Chabrier (2003) IMF for the mass and SFR.

Although a negative trend exists between $\Delta[12 + \log(\mathrm{O/H})]_{\mathrm{M10}}$ and stellar mass, we note that there is no trend with SFR in Fig. 6. From the upper-left panel of Fig. 6, taken in combination, we see a similar trend between $\Delta[12 + \log(\mathrm{O/H})]_{\mathrm{M10}}$ and mass in the FMR residuals of the Erb et al. (2006), Richard et al. (2011), Wuyts et al. (2012), Christensen et al. (2012) and Belli et al. (2013) samples. In their analysis, Belli et al. (2013) note the discrepancy between their data and the original $z \sim 0.1$ FMR of Mannucci et al. (2010) and act to remove it by comparing to the low-mass regime version of the FMR presented in Mannucci et al. (2011) instead. However, when we compare the HiZELS-FMOS sample to the Mannucci et al. (2011) FMR, the trend between $\Delta[12 + \log(\mathrm{O/H})]$ and stellar mass is reduced but still remains with a scatter of 0.3 dex. It therefore appears that the trend between $\Delta[12 + \log(\mathrm{O/H})]_{\mathrm{M10}}$ and the mass component of the FMR is driven by the observed flattening in the mass–metallicity relation, at all SFRs, for the HiZELS-FMOS sample (see Fig. 5).

To describe the plane in mass, metallicity and SFR we observe for the HiZELS galaxies at $z = 0.84$–1.47 and remove the trend between $\Delta[12 + \log(\mathrm{O/H})]$ and stellar mass, we perform a fit to the FMOS data of the same form as Mannucci et al. (2010), that is

$$12 + \log(\mathrm{O/H}) = a_0 + a_1\,m + a_2\,s + a_3\,m^2 + a_4\,ms + a_5\,s^2, \quad (6)$$

where $m = \log M_\star - 10$ and $s = \log$ SFR. This is a fit to only 108 $z = 0.84$–1.47 galaxies (as we include both the 64 [N II] detected galaxies and the 44 upper limits), unlike the $\sim$140 000 galaxies used for calculating the Mannucci et al. (2010) FMR, hence we force the parameters a_i to have the same sign as that of Mannucci et al. (2010) to maintain a similar surface form. The best-fitting parameters are given in Table 2. Forcing the parameters to keep the same sign as their Mannucci et al. (2010) equivalents means that a_1 (a_3) becomes zero in the fitting process which, as it was positive (negative) in the Mannucci et al. (2010) FMR, is its minimum (maximum) allowed value. Hereafter, we refer to the fit to our HiZELS-FMOS data as the high-redshift fundamental metallicity relation (HzFMR).

The lower two panels of Fig. 6 show the residuals in metallicity about this new HzFMR plane, $\Delta[12 + \log(\mathrm{O/H})]_{\mathrm{HzFMR}}$. For the HiZELS-FMOS data, the trend between the residuals and the stellar mass is now removed and the scatter about this plane is

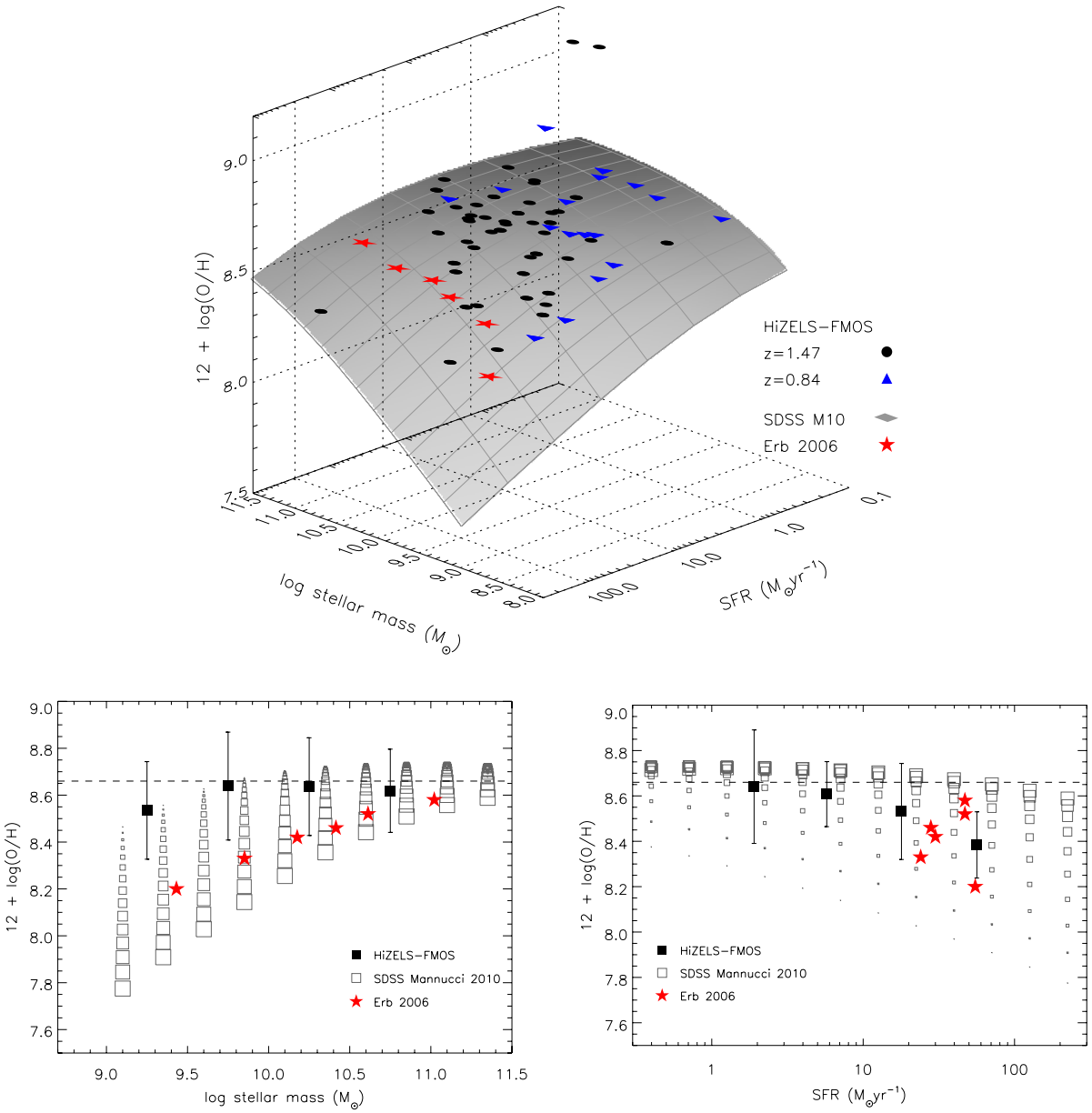

Figure 5. Upper: the three dimensional stellar mass–metallicity–SFR plane. The blue filled triangles and black filled circles are the HiZELS-FMOS data at $z = 0.84$ and 1.47, respectively. The grey surface represents the low-redshift SDSS FMR surface of Mannucci et al. (2010), M10, which we have converted to a Pettini & Pagel (2004) metallicity calibration. The red stars are the median values from Erb et al. (2006) at $z \sim 2$. Lower left: a projection of the 3D plane to show just the mass–metallicity relation. In this plot, the black filled squares and their associated scatter (*one standard deviation*) show the median metallicity values per mass bin (including those derived from the [N II] upper limits). The size of the open grey squares representing the Mannucci et al. (2010) FMR corresponds to their SFR, with the smallest and largest squares having $\log \mathrm{SFR} = -0.9$ and 2.35, respectively, with each consecutive square size separated by 0.25 dex. The black dashed horizontal line is the solar value of 8.66 (Asplund et al. 2004). Lower right: a projection of the 3D plane to show just the SFR–metallicity relation. Again the black filled squares and their associated scatter are the median metallicity values per SFR bin. The size of the open grey squares representing the Mannucci et al. (2010) FMR corresponds to their stellar mass, with the smallest and largest squares having $\log M_\star = 9.0$ and 11.25, respectively, with each consecutive square size separated by 0.25 dex. This figure demonstrates that the HiZELS-FMOS galaxies are in broad agreement with *both* the $z \sim 0.1$ plane of Mannucci et al. (2010) *and* the $z = 2$ observations of Erb et al. (2006) due to the shape of the FMR.

reduced significantly from 0.4 dex to 0.2 dex, when compared to the HiZELS-FMOS residuals around the Mannucci et al. (2010) FMR. The scatter is broadly consistent with the measurement errors which are typically 0.06 dex but are in the range 0.01–0.2 dex so there is no strong evidence that this scatter is driven by trends with additional galaxy properties. We note that the trend between $\Delta[12 + \log(\mathrm{O/H})]$ and stellar mass is also removed from the comparison samples of Richard et al. (2011) and Wuyts et al. (2012) with their combined scatter falling from 0.3 dex for the Mannucci et al. (2010) FMR to 0.2 dex for our HzFMR plane, despite being excluded from the fitting process.

5 DISCUSSION AND SUMMARY

The main result of this paper is that star-forming galaxies at $z = 0.84$–1.47 are on average no less metal abundant than galaxies

Table 2. The parameters used in equation (6) to fit a plane in mass, metallicity and SFR. The HzFMR is a plane fitted to the HiZELS-FMOS data, including the upper limits from the non-detections of [N II]. For comparison we also include the parameters we find from a fit to the Mannucci et al. (2010) $z \sim 0.1$ SDSS FMR after we convert it to a Pettini & Pagel (2004) metallicity calibration.

Plane	Fit parameters					
	a_0	a_1	a_2	a_3	a_4	a_5
HzFMR	8.77	0.00	−0.055	0.000	0.019	−0.101
SDSS FMR_{PP04}	8.58	0.24	−0.092	−0.127	0.085	−0.034

of similar mass and SFR at $z \sim 0.1$, contrary to results from earlier studies of the evolution of the mass–metallicity relation (e.g. Erb et al. 2006; Maiolino et al. 2008; Yabe et al. 2012; Zahid et al. 2013), which were likely driven in part by the higher average SFRs of their galaxies. In fact the mass–metallicity relation for the HiZELS-FMOS sample is in remarkable agreement with the low-redshift relations of Tremonti et al. (2004) and Kewley & Ellison (2008). However, we note that Zahid et al. (2012) do see an evolution to lower metallicities at $z = 0.8$ compared to local studies, for a rest-frame UV–optical, photometrically selected sample that includes galaxies in a similar SFR range as the HiZELS-FMOS. A UV selection tends to bias against metal-rich/dusty galaxies while being complete for very metal poor galaxies, which may be the reason for this discrepancy. We also find good evidence that a relationship between mass, metallicity and SFR similar to, but not the same as, the FMR described at low redshift by Mannucci et al. (2010) is also present at $z = 0.84$–1.47. This is the first demonstration of the presence of such a plane *at* $z \gtrsim 1$ for a well-defined sample of star-forming galaxies with a range of SFRs and masses.

The simple theoretical explanation for the shape of the FMR is that it is the competing effects of chemical enrichment of the gas by the evolving stellar population, star formation-driven winds and the inflow of IGM gas (e.g. Davé et al. 2011). The correlation between mass and gas phase metallicity is explained, to first order, by strong star formation-driven winds driving enriched gas out of lower mass galaxies (Larson 1974). The anticorrelation between SFR and metallicity is due to the fuel for new star formation being cool, relatively metal-poor gas inflowing from the IGM (e.g.

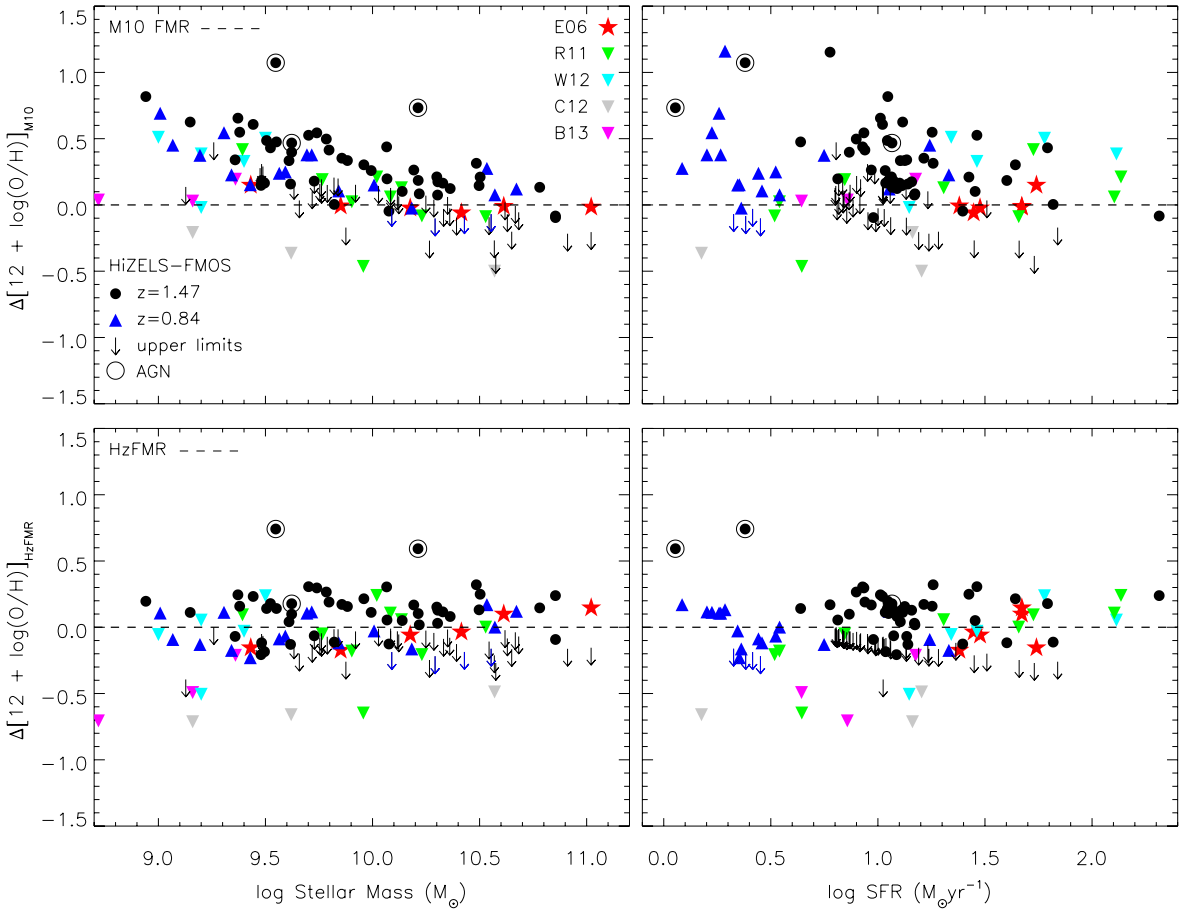

Figure 6. Upper: the difference between measured metallicity and that predicted by the FMR of Mannucci et al. (2010) ($\Delta[12 + \log(O/H)]_{M10}$) plotted against stellar mass (left) and SFR (right). Positive values are metallicities higher than that expected by the FMR. The HiZELS-FMOS points are represented by black circles ($z = 1.47$) and blue triangles ($z = 0.84$). The HiZELS-FMOS galaxies are found to scatter around the $z \sim 0.1$ FMR although there is a negative trend between $\Delta[12 + \log(O/H)]_{M10}$ and stellar mass. The open circles denote likely AGN based on the BPT diagram or those with $\log([N\,II]/H\alpha) > 0.2$ (see Fig. 3). The downward arrows are upper limits for galaxies without detected [N II]. We include the median values of Erb et al. (2006) (red stars) and the individual lensed galaxies from Richard et al. (2011), Wuyts et al. (2012), Christensen et al. (2012) and Belli et al. (2013) represented by green, cyan, grey and magenta inverted triangles, respectively. Lower: the difference between measured metallicity and that predicted by our best-fitting HzFMR plane to the HiZELS-FMOS data ($\Delta[12 + \log(O/H)]_{HzFMR}$, see equation 6) plotted against stellar mass (left) and SFR (right). The negative trend between $\Delta[12 + \log(O/H)]$ is now removed and the scatter significantly reduced.

Finlator & Davé 2008). Although our observed metallicities scatter around the $z \sim 0.1$ FMR of Mannucci et al. (2010) we observe a flattening of the mass–metallicity relation, at all SFR, which leads to greater disagreement with the FMR at high and low masses (Fig. 6). We fit our own plane to the HiZELS-FMOS data, the HzFMR, which accounts for this flattening, providing better agreement with our data and similar studies. We speculate that the reason for the observed flattening in the mass–metallicity relation is that at earlier times the FMR is in its infancy so the balance of gas inflow and outflow may have not yet set up the steeper relation at higher SFR.

We observe a negative correlation between SFR and metallicity in the HzFMR, which is consistent with the picture that the elevated SFRs of typical galaxies at $z \gtrsim 1$ are caused by the increased efficiency of metal-poor IGM gas inflow (e.g. Kereš et al. 2005; Bower et al. 2006; Dekel, Sari & Ceverino 2009). This enhanced gas inflow is the likely cause of the increase in the observed SFRD of the Universe (Lilly et al. 1996; Madau et al. 1996; Sobral et al. 2013), and it is therefore not driven by major mergers (as we also demonstrated through direct observation in Sobral et al. 2009 and Stott et al. 2013), which may instead act to maintain or enhance the metallicity of the gas, not dilute it.

Through the inclusion of Hβ and [O III] observations we estimate the dust content and AGN fraction of our HIZELS-FMOS sample. The average dust attenuation in the V band and at the wavelength of Hα (6563 Å) are found, through the Balmer decrement, to be $A_V = 1.3 \pm 0.2$ and $A_{\rm H\alpha} = 1.1 \pm 0.2$, respectively. This is in agreement with the $A_{\rm H\alpha} = 1$ used throughout this paper and for HiZELS papers such as Sobral et al. (2013) and Stott et al. (2013).

We use the BPT diagram (Baldwin et al. 1981) to estimate the potential AGN fraction and find it to be consistent with low-redshift samples with ∼10 per cent of the galaxies occupying the region of the BPT diagram found to contain AGN, using the Kewley et al. (2001) definition, in agreement with independent, multiwavelength analyses of the HiZELS (Garn et al. 2010; Sobral et al. 2013).

In conclusion, this study is the first of its kind to demonstrate the presence of the FMR, or a variant of it (the HzFMR), at $z \gtrsim 1$ with a well-understood sample of typical star-forming galaxies. This means that the bulk of the metal enrichment for the $z \sim 1$–1.5 star-forming galaxy population takes place in the 4 Gyr before $z = 1.5$. The challenge for galaxy evolution theory is to explain how this balance between the competing processes of gas inflow and outflow creates a mass, metallicity and SFR plane by at least $z = 1.5$. Taken in concert with our results from Sobral et al. (2013) and Stott et al. (2013), that there is little evolution in the mass, size and merger rates of the star-forming galaxy population since $z \sim 2$, this lack of change in the gas phase metallicity is further evidence that, *taken as a population*, many of the properties of star-forming galaxies have remained remarkably constant over ∼9 Gyr of cosmic time, despite the significant change in typical SFR. We speculate that the negative slope of the SFR–metallicity component of the HzFMR plane, combined with the lack of evolution in the number density of major mergers for star-forming galaxies (Stott et al. 2013), demonstrates that it is the efficient inflow of metal-poor gas from the IGM that leads to this increase in typical SFR with redshift and is ultimately responsible for the rise in the SFRD of the Universe at $z \gtrsim 1$.

ACKNOWLEDGEMENTS

The authors wish to thank Kentaro Aoki for technical assistance and Fabrice Durier for useful discussions. JPS, RGB and IRS acknowledge support from the UK Science and Technology Facilities Council (STFC) under ST/I001573/1. DS acknowledges the award of a Veni Fellowship. IRS acknowledges support from a Leverhulme Fellowship, the ERC Advanced Investigator programme DUSTYGAL and a Royal Society/Wolfson Merit Award. TK acknowledges financial support by a Grant-in-Aid for the Scientific Research (nos 23740144; 24244015) by the Japanese Ministry of Education, Culture, Sports and Science.

Based on data collected at the Subaru Telescope, which is operated by the National Astronomical Observatory of Japan.

The United Kingdom Infrared Telescope is operated by the Joint Astronomy Centre on behalf of the Science and Technology Facilities Council of the UK.

REFERENCES

Abazajian K. N. et al., 2009, ApJS, 182, 543
Alloin D., Collin-Souffrin S., Joly M., Vigroux L., 1979, A&A, 78, 200
Arimoto N., Yoshii Y., 1987, A&A, 173, 23
Asplund M., Grevesse N., Sauval A. J., Allende Prieto C., Kiselman D., 2004, A&A, 417, 751
Baldwin J. A., Phillips M. M., Terlevich R., 1981, PASP, 93, 5
Belli S., Jones T., Ellis R. S., Richard J., 2013, ApJ, 772, 141
Benson A. J., Bower R. G., Frenk C. S., Lacey C. G., Baugh C. M., Cole S., 2003, ApJ, 599, 38
Best P. et al., 2010, preprint (arXiv:1003.5183)
Bower R. G., Benson A. J., Malbon R., Helly J. C., Frenk C. S., Baugh C. M., Cole S., Lacey C. G., 2006, MNRAS, 370, 645
Bruzual G., Charlot S., 2003, MNRAS, 344, 1000
Calzetti D., Armus L., Bohlin R. C., Kinney A. L., Koornneef J., Storchi-Bergmann T., 2000, ApJ, 533, 682
Casali M. et al., 2007, A&A, 467, 777
Chabrier G., 2003, PASP, 115, 763
Christensen L. et al., 2012, MNRAS, 427, 1953
Crain R. A. et al., 2009, MNRAS, 399, 1773
Cresci G., Mannucci F., Sommariva V., Maiolino R., Marconi A., Brusa M., 2012, MNRAS, 421, 262
Davé R., Finlator K., Oppenheimer B. D., 2011, MNRAS, 416, 1354
Davé R., Finlator K., Oppenheimer B. D., 2012, MNRAS, 421, 98
Dayal P., Ferrara A., Dunlop J. S., 2013, MNRAS, 430, 2891
Dekel A., Sari R., Ceverino D., 2009, ApJ, 703, 785
Denicoló G., Terlevich R., Terlevich E., 2002, MNRAS, 330, 69
Domínguez A. et al., 2013, ApJ, 763, 145
Erb D. K., Shapley A. E., Pettini M., Steidel C. C., Reddy N. A., Adelberger K. L., 2006, ApJ, 644, 813
Finlator K., Davé R., 2008, MNRAS, 385, 2181
Garn T. et al., 2010, MNRAS, 402, 2017
Geach J. E., Smail I., Best P. N., Kurk J., Casali M., Ivison R. J., Coppin K., 2008, MNRAS, 388, 1473
Geach J. E., Sobral D., Hickox R. C., Wake D. A., Smail I., Best P. N., Baugh C. M., Stott J. P., 2012, MNRAS, 426, 679
Iwamuro F. et al., 2012, PASJ, 64, 59
Kennicutt R. C., Jr, 1998, ARA&A, 36, 189
Kereš D., Katz N., Weinberg D. H., Davé R., 2005, MNRAS, 363, 2
Kewley L. J., Dopita M. A., 2002, ApJS, 142, 35
Kewley L. J., Ellison S. L., 2008, ApJ, 681, 1183
Kewley L. J., Dopita M. A., Sutherland R. S., Heisler C. A., Trevena J., 2001, ApJ, 556, 121
Kimura M. et al., 2010, PASJ, 62, 1135
Lamareille F. et al., 2009, A&A, 495, 53
Lara-López M. A. et al., 2010, A&A, 521, L53
Lara-López M. A. et al., 2013, MNRAS, 434, 451
Larson R. B., 1974, MNRAS, 169, 229
Lequeux J., Peimbert M., Rayo J. F., Serrano A., Torres-Peimbert S., 1979, A&A, 80, 155
Lilly S. J., Le Fevre O., Hammer F., Crampton D., 1996, ApJ, 460, L1

Lilly S. J., Carollo C. M., Pipino A., Renzini A., Peng Y., 2013, ApJ, 772, 119
Ly C., Lee J. C., Dale D. A., Momcheva I., Salim S., Staudaher S., Moore C. A., Finn R., 2011, ApJ, 726, 109
Madau P., Ferguson H. C., Dickinson M. E., Giavalisco M., Steidel C. C., Fruchter A., 1996, MNRAS, 283, 1388
Maiolino R. et al., 2008, A&A, 488, 463
Mannucci F., Cresci G., Maiolino R., Marconi A., Gnerucci A., 2010, MNRAS, 408, 2115 (M10)
Mannucci F., Salvaterra R., Campisi M. A., 2011, MNRAS, 414, 1263
Matsuda Y. et al., 2011, MNRAS, 416, 2041
Momcheva I. G., Lee J. C., Ly C., Salim S., Dale D. A., Ouchi M., Finn R., Ono Y., 2013, AJ, 145, 47
Newman S. F. et al., 2013, preprint (arXiv:1306.6676)
Osterbrock D. E., 1989, Astrophysics of Gaseous Nebulae and Active Galactic Nuclei. University Science Books, Mill Valley, CA
Pence W., 1999, in Mehringer D. M., Plante R. L., Roberts D. A., eds, ASP Conf. Ser. Vol. 172, Astronomical Data Analysis Software and Systems VIII. Astron. Soc. Pac., San Francisco, p. 487
Pérez-Montero E. et al., 2009, A&A, 495, 73
Pettini M., Pagel B. E. J., 2004, MNRAS, 348, L59
Rayner J. T., Cushing M. C., Vacca W. D., 2009, ApJS, 185, 289
Richard J., Jones T., Ellis R., Stark D. P., Livermore R., Swinbank M., 2011, MNRAS, 413, 643
Rodrigues M. et al., 2012, Proc. SPIE, 8450, 84503H
Roseboom I. G. et al., 2012, MNRAS, 426, 1782
Rousselot P., Lidman C., Cuby J.-G., Moreels G., Monnet G., 2000, A&A, 354, 1134
Salpeter E. E., 1955, ApJ, 121, 161
Sánchez S. F. et al., 2013, A&A, 554, A58
Savaglio S. et al., 2005, ApJ, 635, 260
Skrutskie M. F. et al., 2006, AJ, 131, 1163
Sobral D. et al., 2009, MNRAS, 398, 75
Sobral D., Best P. N., Geach J. E., Smail I., Cirasuolo M., Garn T., Dalton G. B., Kurk J., 2010, MNRAS, 404, 1551
Sobral D., Best P. N., Smail I., Geach J. E., Cirasuolo M., Garn T., Dalton G. B., 2011, MNRAS, 411, 675
Sobral D., Best P. N., Matsuda Y., Smail I., Geach J. E., Cirasuolo M., 2012, MNRAS, 420, 1926
Sobral D., Smail I., Best P. N., Geach J. E., Matsuda Y., Stott J. P., Cirasuolo M., Kurk J., 2013, MNRAS, 428, 1128
Stott J. P., Sobral D., Smail I., Bower R., Best P. N., Geach J. E., 2013, MNRAS, 430, 1158
Tremonti C. A. et al., 2004, ApJ, 613, 898
Villar V., Gallego J., Pérez-González P. G., Pascual S., Noeske K., Koo D. C., Barro G., Zamorano J., 2008, ApJ, 677, 169
White S. D. M., Rees M. J., 1978, MNRAS, 183, 341
Wright S. A., Larkin J. E., Graham J. R., Ma C.-P., 2010, ApJ, 711, 1291
Wuyts E., Rigby J. R., Sharon K., Gladders M. D., 2012, ApJ, 755, 73
Yabe K. et al., 2012, PASJ, 64, 60
Zahid H. J., Kewley L. J., Bresolin F., 2011, ApJ, 730, 137
Zahid H. J., Dima G. I., Kewley L. J., Erb D. K., Davé R., 2012, ApJ, 757, 54
Zahid H. J., Geller M. J., Kewley L. J., Hwang H. S., Fabricant D. G., Kurtz M. J., 2013, ApJ, 771, L19

This paper has been typeset from a TEX/LATEX file prepared by the author.